

# Effect of holmium doping on the structure and photocatalytic behavior of TiO<sub>2</sub>-based nanosheets

Xinzhao Liu · Pengfei Fang · Yang Liu ·  
Zhi Liu · Dingze Lu · Yuanpeng Gao ·  
Feitai Chen · Dahai Wang · Yiqun Dai

Received: 9 May 2014 / Accepted: 28 July 2014 / Published online: 12 August 2014  
© Springer Science+Business Media New York 2014

**Abstract** A series of holmium-doped TiO<sub>2</sub>-based nanosheet (Ho-TNS) photocatalysts with different Ho/Ti molar ratios were prepared via a simple hydrothermal method. The photocatalysts were characterized by field-emission scanning electron microscope, high-resolution transmission electron microscope, X-ray diffraction (XRD), Raman Spectroscopy, X-ray photoemission spectroscopy, nitrogen adsorption–desorption isotherm measurement, ultraviolet–visible light diffuse reflectance spectra (DRS), and fluorescence spectra (FL). The TEM images of Ho-TNS exhibit clearly sheet-like structures and existence of the (201) plane of H<sub>2</sub>Ti<sub>3</sub>O<sub>7</sub>. The increased (101) peak intensity in XRD spectrum and the enhanced  $E_g$  mode (141 cm<sup>-1</sup>) in Raman spectrum indicate that Ho doping has obvious influence on the formation and structure of Ho-TNS, which can be explained by the formation of Ho–O–Ti bonds. With the doping ratio (Ho/Ti molar ratio) increasing from 0 to 2.0 %, the absorption edge shifts to a longer wavelength, and the band-gap of photocatalysts reduces from 3.18 to 3.07 eV. The decline of FL intensity implies that the photocatalysts with higher Ho content have higher electron–hole separation efficiency. However, after Ho doping, the surface structure of specimens is significantly altered, which will lead to the specific surface areas and adsorption

capacity decrease. Under the combined effect of the variables, the photocatalyst with a doping ratio of 1.0 % reaches the best photoactivity, which is 1.90-fold and 12.38-fold higher compared with undoped TNS and P25 under visible light, respectively. The high photoactivity of the prepared Ho-TNS indicates that it may be useful for dealing with wastewater.

## Introduction

As one of the photosensitive semiconductors, titanium dioxide (TiO<sub>2</sub>) has been widely used in the degradation of dyes and pollutants in wastewater and air [1]. It has shown various promising aspects such as its outstanding activity, chemical stability, low-cost preparation, low toxicity, no second pollution, and other unique properties [2, 3]. While the fine TiO<sub>2</sub> powders have been proved to be an effective photocatalyst to solve environment problems, some drawbacks in their practical applications still exist which is worth further studying. Typical examples include the low separation and migration efficiency of electron–hole pairs, the narrow range of absorbing light, and the poor adsorption capacity toward some organic molecules.

A lot of attempts have been made to prepare TiO<sub>2</sub>-based photocatalyst with high separation efficiency of electron–hole pairs. For example, a series of TiO<sub>2</sub> nanostructures (e.g., nanorods [4, 5], nanowires [6], nanotubes [7, 8], nanosheets [9–11], and nanofibers [12]) have been prepared by morphological control methods. Among these TiO<sub>2</sub> nanostructures, nanosheets possess high specific surface area and small thickness. These characteristics assure nanosheets' potential to be exposed to more light and contact with more dye molecules. Meanwhile, its separation and migration efficiency of photogenerated

X. Liu · P. Fang (✉) · Y. Liu · Z. Liu · D. Lu · Y. Gao ·  
F. Chen · Y. Dai  
Department of Physics and Key Laboratory of Artificial  
Micro- and Nano-structures of Ministry of Education, Wuhan  
University, Wuhan 430072, China  
e-mail: fangpf@whu.edu.cn

D. Wang (✉)  
School of Physics and Technology, Wuhan University,  
Wuhan 430072, China  
e-mail: dhwang@whu.edu.cn

electron and hole pairs is effectively improved. These advantages make nanosheets be expected to exhibit high photoactivity. Hydrothermal method is known as a simple and convenient way to prepare nanosheets. For example, Yao et al. [13] has proved that the hydrothermal reaction of  $\text{TiO}_2$  under high-concentration alkali condition is a transformation from 3D to 2D and eventually 1D, which means the nanotubes prepared by hydrothermal method are curly nanosheets. By controlling the hydrothermal reaction parameters (e.g., reaction time, the alkali species, and alkali concentration), Chen et al. [9–11] has prepared uniform,  $\text{TiO}_2$ -based nanosheets (TNS) with higher photoactivities in degradation of RhB than P25. The excellent photoactivity of TNS can be attributed to the large surface area and the fast migration of electron–hole pairs [9, 10, 14].

However, the prepared TNS also exhibit some shortcomings (e.g., the narrow range of absorbing light and the low separation efficiency of electron–hole pairs). Various methods have been attempted to modify the regular  $\text{TiO}_2$  photocatalyst, such as hybrid compositing [15], ion doping [16], dye sensitization [17], and metal loading [18], which can be used to solve the shortcomings of TNS as well. Ions doping, especially rare earth metal ions doping [19–21], has been proved to improve the photoactivity of  $\text{TiO}_2$  [22–24]. This is because rare earth metal ions with incompletely occupied 4f and empty 5d orbitals often serve as a catalyst or promote catalysis [25]. Cerium doping TNS (Ce-TNS) have been prepared in our previous work [26], which showed significantly enhanced photoactivity under UV light irradiation. But the visible light photoactivity of Ce-TNS was reduced because cerium has two kinds of valence states ( $\text{Ce}^{3+}/\text{Ce}^{4+}$ ), the doped cerium had trapped a large part of electrons from RhB. Hence, a certain rare earth metal with only one valence state, such like holmium (Ho) et al., may be used as a dopant to enhance the visible light photoactivity of TNS. Some researches have reported that Ho doping can effectively improve the UV light photoactivity of  $\text{TiO}_2$  photocatalyst. Cai et al. [27] have proved that Ho has the ability to improve the photoactivity of  $\text{TiO}_2$  due to the enhancement of photogenerated electron–hole pair separation. Research by Zhou et al. [6] shows that Ho-doped  $\text{TiO}_2$  nanowires exhibit excellent photoactivity due to the synergetic effects of small crystallite size, large surface area, and charge imbalance. However, the investigation on Ho doping to improve the visible light photoactivity of  $\text{TiO}_2$  has rarely been reported, which is still a tough challenge.

In this work, firstly a series of Ho-doped  $\text{TiO}_2$ -based nanosheets (Ho-TNS) were prepared by hydrothermal method under alkaline conditions. Then, the adsorption capacities and photoactivities of Ho-TNS for the degradation of RhB were investigated. Moreover, the possible

electron transfer mechanisms were discussed. And the investigation on Ho doping in TNS and the effect of Ho doping on the structure and photocatalytic behavior of TNS deserve further study.

## Experimental

### Synthesis of Ho-doped $\text{TiO}_2$ -based nanosheets

$\text{Ho}_2\text{O}_3$  (purchased from National Engineering Research Centre of Rare Earth Metallurgy and Function Materials, analytical pure) were dissolved in heated 3 mol/L  $\text{HNO}_3$  solution to get 0.1 mol/L Ho nitrate solution, which was chosen as the Ho precursor. 0.8 g of P25 powders (purchased from Degussa Co., Ltd.) were dispersed in 50 mL of 10 mol/L NaOH solution. Appropriate amount of Ho nitrate solution was dropped into the suspension slowly. After 40-min magnetic stirring, the mixture was transferred into a Teflon autoclave (100 mL) and heated at 130 °C for 3 h. After the autoclave had been water-cooled to the ambient temperature, the resultant powders were separated by high-speed centrifugation and washed by de-ionized water for several times until the pH value of the rinsed water reached about seven. Then, the powder was added into 200 mL of 0.1 mol/L HCl and magnetic stirred for 1 h to get a complete proton exchange. After the acid treatment, the powders were washed again until pH value of the rinsed water reached about seven. Finally, the specimens were put in a drying oven at 70 °C for 12 h. A series of Ho-TNS were prepared by changing the amount of Ho nitrate solution added. The specimens were denoted as X % Ho-TNS according to the Ho/Ti molar ratios ( $X = 0.1, 0.25, 0.5, 0.75, 1.0, 1.25, \text{ and } 2.0$ ). As a comparison, undoped TNS was prepared under the same condition except adding Ho nitrate solution. NaOH,  $\text{HNO}_3$ , and HCl were analytically pure and used without further purification.

### Characterizations

The morphological features of the specimens were characterized by field-emission scanning electron microscope (FESEM, Hitachi S-4800), transmission electron microscopy (TEM, JEOL JEM-2010 [HT]), and high-resolution transmission electron microscopy (HRTEM, JEM-2010 FEF) with an energy dispersive spectroscope (EDS). The XRD patterns were obtained by a Bruker D8 advance X-ray diffractometer using monochromatic  $\text{Cu K}\alpha$  radiation ( $\lambda = 1.5406 \text{ \AA}$ ). The accelerating voltage and current were 40 kV and 40 mA, respectively. The structures of specimens were measured by Raman spectrometer (Horiba LabRAM HR), with excitation wavelength of 488 nm and output power of 5 mW. X-ray photoemission spectroscopy

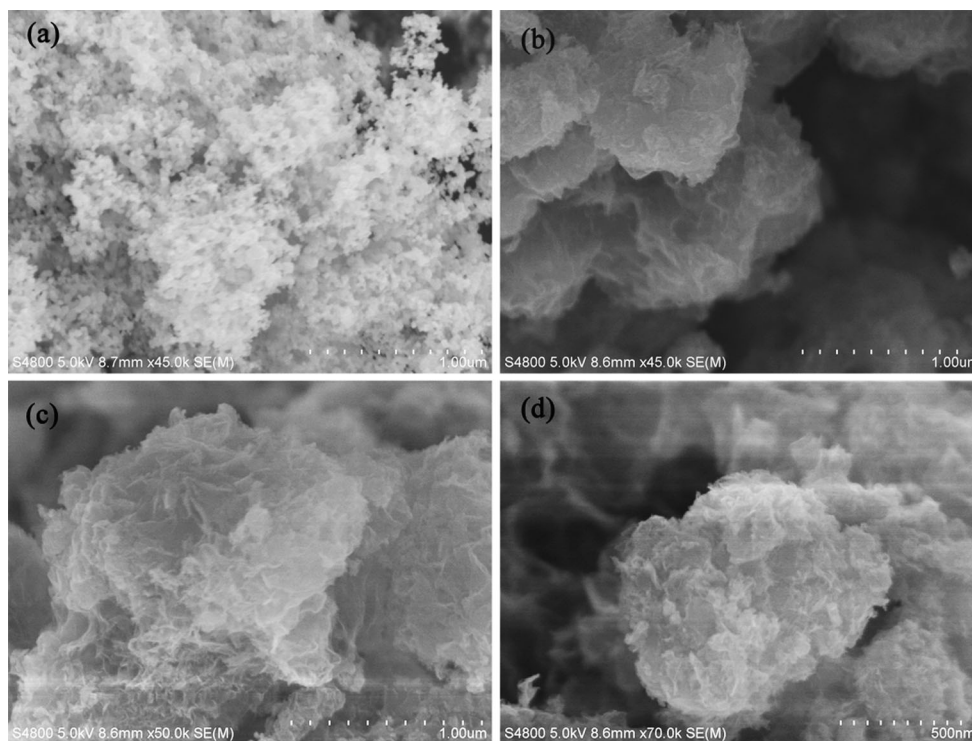


**Fig. 1** FESEM images of P25 (a), undoped TNS (b), 1.0 % Ho-TNS (c), and 2.0 % Ho-TNS (d)

(XPS) measurements were collected on a Thermo VG Multilab2000 using Al K $\alpha$  as the excitation source. The Brunauer-Emmett-Teller specific surface areas ( $S_{\text{BET}}$ ) of the specimens were determined by nitrogen adsorption-desorption isotherm measurements at 77 K on a JW-BK instrument. Ultraviolet-visible (UV-vis) light DRS were collected on a Shimadzu UV-2550 spectrophotometer with integrating sphere attachment using barium sulfate as a reference. A Hitachi FL4600 fluorescence spectrometer (FL) with 500 V voltage and 205 nm excitation wavelength was used to study the recombination efficiency of electrons and holes. The record was ranging from 450 to 520 nm.

#### Photocatalytic performance evaluations

The photoactivities of the specimens were performed under a 160 W high-pressure mercury lamp with 20 mg/L RhB (product of Sinopharm Group Co., Ltd.) as the target pollutant. 0.10 g of specimens were suspended in 100 mL of aqueous solution of RhB. One hour of adsorption time in dark condition was allowed before exposure to light irradiation, and the residual concentration of RhB was determined to evaluate the adsorption capacity of specimens. Water tank was used to slow down the increase of temperature during irradiation. Every 30 min, 1.6 mL of the suspension was withdrawn, centrifuged and analyzed for

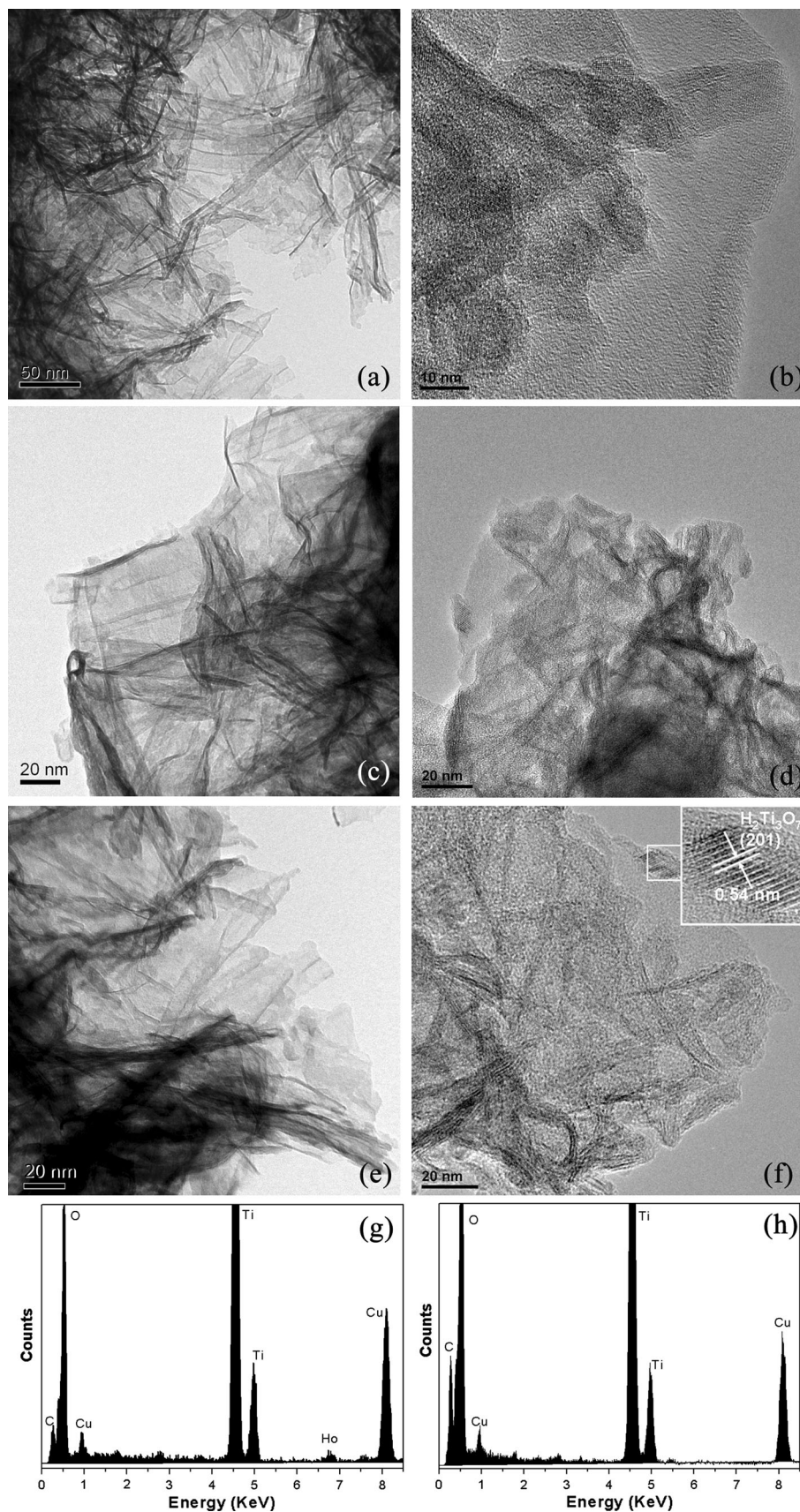
residual RhB concentration by UV-vis absorbance spectra. Visible light photocatalytic reaction was done under the same condition with a cutoff filter ( $\lambda > 400$  nm) covering the beaker.

## Results and discussion

### Characterization results

Figure 1 shows the FESEM images of P25 and the prepared specimens. The raw P25 nanoparticles (average diameter of about 20 nm) can be seen clearly in Fig. 1a. However, the unique nanosheet-like structures are obvious and no P25 nanoparticles are found in Fig. 1b–d, which demonstrate that after hydrothermal process, raw P25 nanoparticles almost convert to the nanosheet-like structure. In order to further study the morphological features of the specimens, TEM and high-resolution TEM images of prepared specimens are shown in Fig. 2. The result is according with the FESEM images. The sheet-like structure can be seen clearly in Fig. 2, and no raw P25 nanoparticles are found in the TEM or HRTEM images. The inset in Fig. 2f clearly shows that the interplanar distance between adjacent lattice planes is ca. 0.54 nm, corresponding to the (201) plane of  $\text{H}_2\text{Ti}_3\text{O}_7$  [11]. Some researches suggest that P25  $\text{TiO}_2$  powders react with NaOH

**Fig. 2** TEM images and energy dispersive spectrometer (EDS) spectra of specimens: **a** TEM image of undoped TNS; **b** HRTEM image of undoped TNS; **c** TEM image of 1.0 % Ho-TNS; **d** HRTEM image of 1.0 % Ho-TNS; **e** TEM image of 2.0 % Ho-TNS; **f** HRTEM image of 2.0 % Ho-TNS; **g** EDS spectrum of 2.0 % Ho-TNS; **h** EDS spectrum of undoped TNS



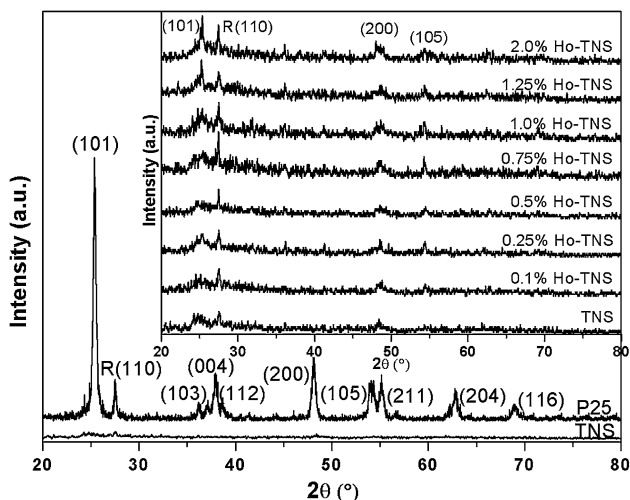


Fig. 3 XRD patterns of P25, undoped TNS, and Ho-TNS

solution to form a highly disordered phase containing  $H_2Ti_3O_7$  nanocrystals [11, 28]. Under the hydrothermal conditions,  $TiO_2$  nanoparticles are stripped into thin lamellar fragments. After the process of stripping develops to a certain extent, large amounts of Ti–O bonds are broken to form  $H_2Ti_3O_7$ . The transformation from  $TiO_2$  to  $H_2Ti_3O_7$  is gradual; it proceeds from surface region and then extends to center region. So, the Ti–O bonds on the surface are broken firstly. During the breaking process of Ti–O bonds, the O atoms are twisted or rotated, creating an angle between Ti and O atoms. It can lead to the formation of the lepidocrocite-type layers, which are suggested to be the construction units in any layered titanate [29]. Then, the thin lamellar fragments link with each other to form larger planar nanosheets [11]. The energy dispersive spectrometer (EDS) was measured in order to find compositional

differences between Ho-TNS and undoped TNS. Figure 2g and h shows the EDS spectra of 2.0 % Ho-TNS and undoped TNS, respectively. The Ti and O elements have been found in both spectra. However, the Ho element located at 6.74 keV can be observed clearly in Fig. 2g only, which can prove the existence of Ho. During the measurement, lacey support films were used to support specimens, which are the source of elements C and Cu.

The XRD patterns of P25, undoped TNS, and Ho-TNS are shown in Fig. 3. The characteristic peaks of anatase and rutile in the XRD of P25 are clear, strong, symmetric, and sharp, which means that the  $TiO_2$  in P25 is mostly crystalline in nature. However, the characteristic peaks in the TNS are obviously broadened, and the intensities are very weak. It indicates that the crystallinity of TNS stays at a low level. The differences between P25 and undoped TNS mean that under the hydrothermal process, the crystallinity of  $TiO_2$  was broken, and a highly disordered phase was formed. In other words, most of P25 powders (crystal) had been converted to nanosheet structure, which implies the accomplishment of transformation from P25 (3D) to nanosheets (2D) [11, 26]. The inset of Fig. 3 shows the XRD spectra of Ho-TNS with different Ho/Ti ratios. It can be seen that the XRD spectra of the specimens with different Ho/Ti ratios are similar. However, with increasing Ho content, there appears to be a corresponding increase in the intensity of (101) peak. The XRD patterns of Ho-TNS suggest that Ho doping can affect the transformation from  $TiO_2$  to  $H_2Ti_3O_7$ .

Raman Spectroscopy is used to further study the structure evolution of Ho-TNS. Obvious changes can be observed at the position of  $141\text{ cm}^{-1}$  in Fig. 4a. The main  $E_g$  mode at  $141\text{ cm}^{-1}$  is arising from the external vibration of the anatase structure [30]. The Raman peaks at 271 and  $449\text{ cm}^{-1}$  are attributed to the break of symmetry in the

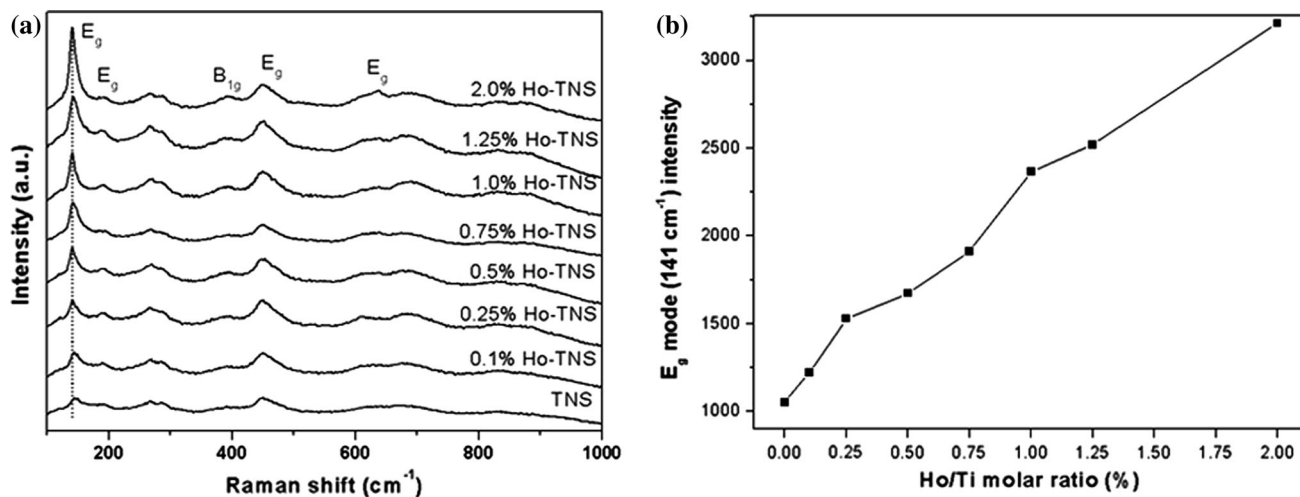
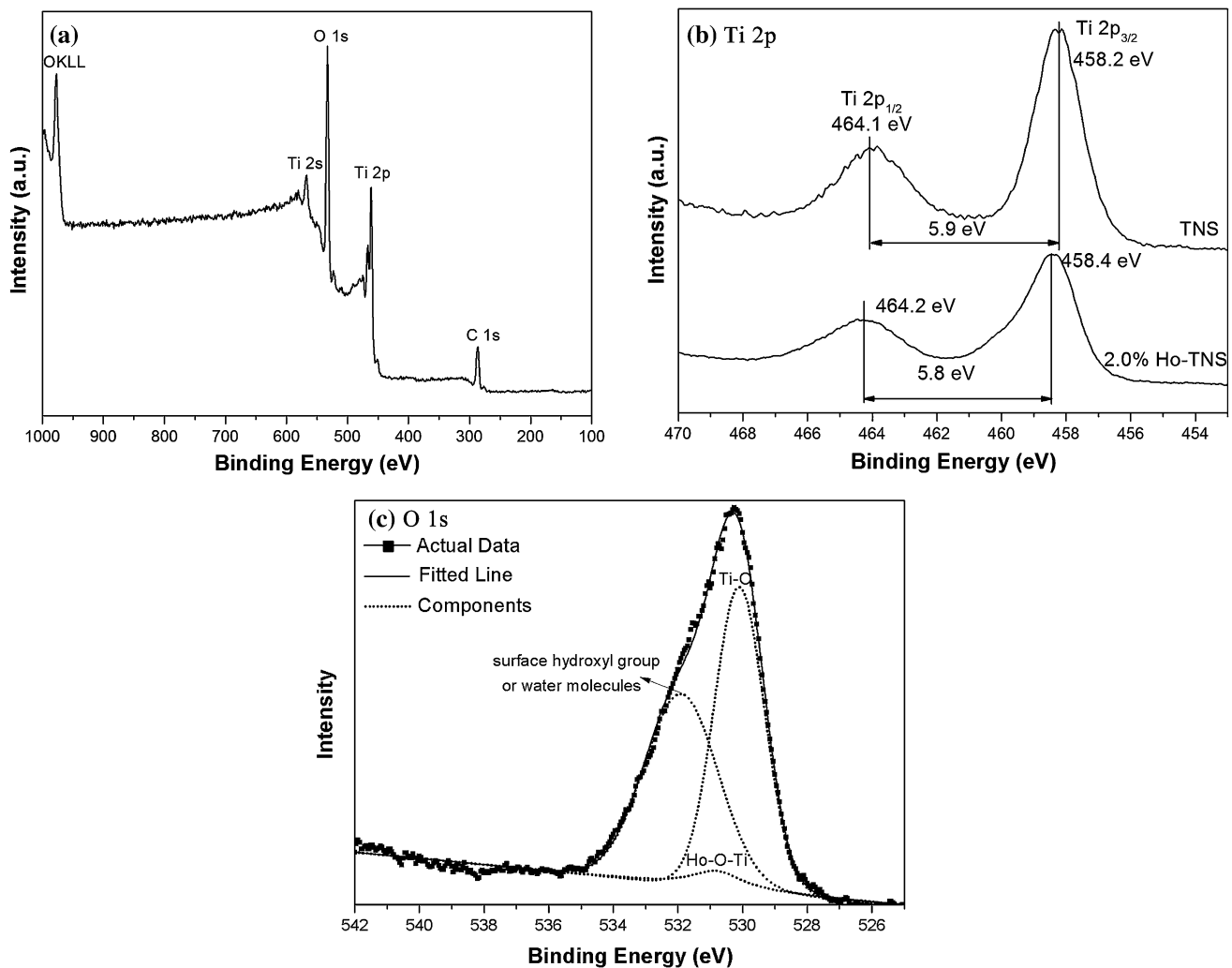


Fig. 4 a Raman spectra of undoped TNS and Ho-TNS; b Raman intensity of  $E_g$  mode ( $141\text{ cm}^{-1}$ ) as a function of doping amount



**Fig. 5** XPS spectra of specimens: **a** survey spectrum of 2.0 % Ho-TNS; **b** Ti 2p peaks in undoped TNS and 2.0 % Ho-TNS; **c** O 1s peaks in 2.0 % Ho-TNS

cent TiO<sub>6</sub> layers [31] and the presence of the 2D lepidocrocite-type TiO<sub>6</sub> octahedral layers [32], respectively. Figure 4b represents the relative intensity of the main  $E_g$  mode (141 cm<sup>-1</sup>) as a function of doping amount. The relative intensity increases linearly with the Ho doping ratio increasing from 0 to 2.0 %. The intensity of  $E_g$  mode of the 2.0 % Ho-TNS is 3.05 times of that of undoped TNS. It indicates that Ho doping can affect the transformation from TiO<sub>2</sub> to H<sub>2</sub>Ti<sub>3</sub>O<sub>7</sub>, which is in accordance with XRD data. We have analyzed the Raman spectra by Lorentzian and Gaussian multi peak fitting. The results show some general trends in the behavior of the full width at half maximum (FWHM) of the main  $E_g$  mode (141 cm<sup>-1</sup>): with Ho content increasing, the FWHM decreases from 16.22 to 14.11 cm<sup>-1</sup>. Figure 4a also indicates the weak frequency shift of the main  $E_g$  mode. The decrease of FWHM and the weak frequency shift of the main  $E_g$  mode suggest that the Ho doping may influence Ti–O lattice vibration.

X-ray photoemission spectroscopy was carried out to determine the chemical composition and valence states of specimens. By assuming that C 1s line lies at 284.6 eV, the calibration of the binding energy was accomplished and the energy shift corrections due to the steady-state charging effect were made. The XPS spectra were fitted by the software of XPS Peak 4.1, and analyzed by performing a Shirley background subtraction. XPS spectra of 2.0 % Ho-TNS and undoped TNS are shown in Fig. 5. Figure 5a is the survey spectrum of 2.0 % Ho-TNS. Figure 5b shows the Ti 2p<sub>1/2</sub> and Ti 2p<sub>3/2</sub> binding energies: for undoped TNS, they are 464.1 and 458.2 eV (space 5.9 eV) and for 2.0 % Ho-TNS they are 464.1 and 458.4 eV (space 5.8 eV), which are in excellent agreement with the literature data for TiO<sub>2</sub> [33]. This result reveals that Ti mainly exists as the chemical state of Ti<sup>4+</sup>. Figure 5c shows the result of the O 1s fit spectra of 2.0 % Ho-TNS which suggests different oxygen environment. The peak at

530.1 eV is due to the  $O^{2-}$  ion in the  $TiO_2$  lattice [34], the peak at 530.8 eV represents the Ho–O–Ti bond [35], and the peak at 531.9 eV should be attributed to the surface hydroxyl group or chemisorbed water molecules on the titania [36]. During the hydrothermal process, Ho are mainly located on the surface of TNS and may affect the transformation from  $TiO_2$  to  $H_2Ti_3O_7$  by two approaches. Firstly, Ho form Ho–O–Ti bonds with the broken Ti–O bonds, which can affect the twisting or rotation of O atoms. Secondly, the formed Ho–O–Ti bonds located on the surface can inhibit the further stripping process of  $TiO_2$  nanoparticles in center region. Thus, formation of lepidocrocite-type layers could be retarded. The XPS results correspond to the XRD and Raman Spectroscopy, which can explain the effect of Ho doping on the structure evolution of Ho-TNS. The variation of the surface area with different specimens is depicted in Fig. 6. After Ho doping,

the  $S_{BET}$  of specimens have the trend to reduce. The reduction of  $S_{BET}$  is another evidence to prove this point. After Ho doping, the transformation from  $TiO_2$  to  $H_2Ti_3O_7$  is retarded, then the process of thin lamellar fragments to link with each other forming larger planar nanosheets is also delayed. The decrease of  $S_{BET}$  can be attributed to the inhibited formation of TNS. However, due to the small amount of doping (<1.0 %),  $S_{BET}$  do not change much.

#### Effect of Ho doping on photoelectric property

Figure 7a shows the UV–vis DRS of specimens, which indicates the influence of Ho doping on the UV–vis absorption. Comparing with the undoped TNS, a red-shift of the absorption profile is observed. The absorption edge shifts to a longer wavelength depending on the content of Ho. In order to signify the specifications of the specimens, the spectra in 350–450 nm are enlarged (inset in Fig. 7a). The results may be attributed to the charge transfer between 4f electrons of Ho ion and the  $TiO_2$  conduction (or valence) band [25]. Moreover, it is noticeable that the light absorption is higher than that of undoped TNS in the range of 400–600 nm, and reinforces with increasing Ho content. This might be ascribed to the broad absorption band of Ho ion [25]. Using the Kubelka–Munk function [37], the band-gap of the  $TiO_2$  material can be calculated by the absorption edge position according to the formula  $E_g = 1240/\lambda$ , where  $\lambda$  is the intersection of the tangent along the absorption edge and wavelength axis. With the doping ratio increasing from 0 to 2.0 %, the band-gap of specimens receives obvious modulation, reducing from 3.18 to 3.07 eV, as shown in Fig. 7b. The ability of response to irradiation is becoming constantly stronger with increasing Ho content, which means that the Ho-TNS may release

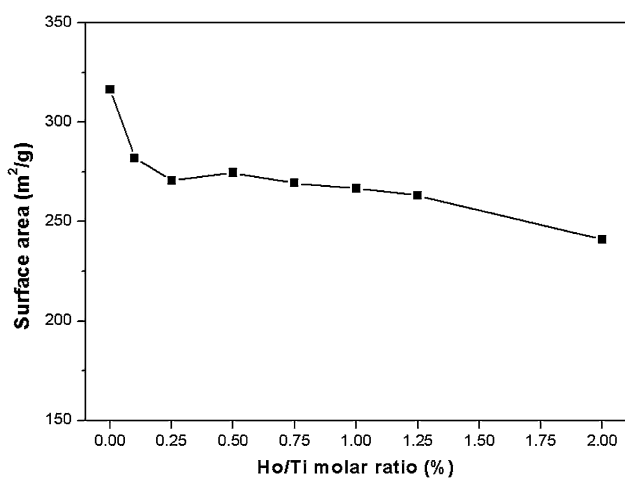


Fig. 6 Surface area of the specimens as a function of doping amount

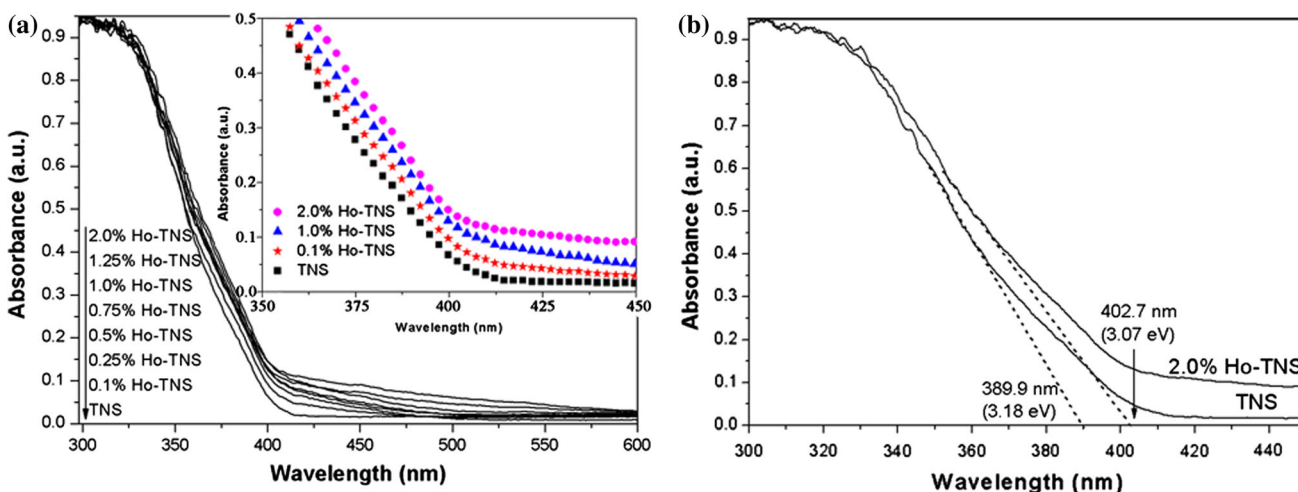
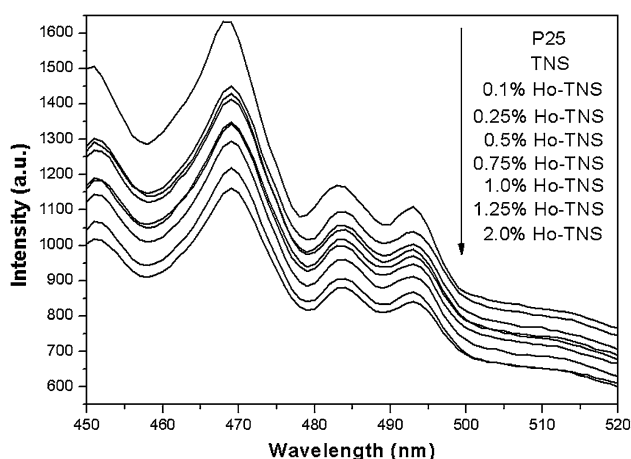
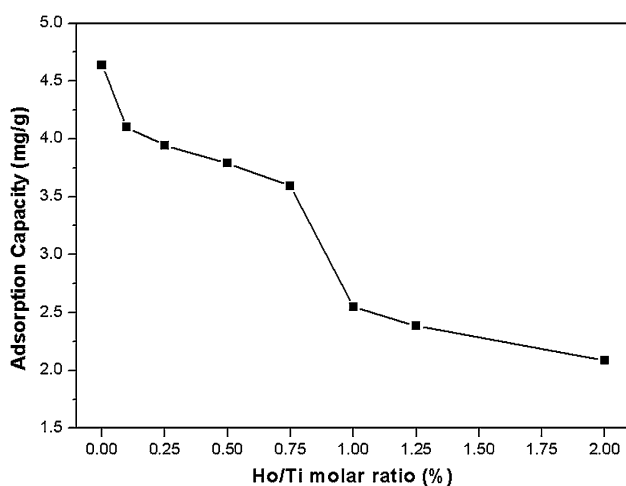


Fig. 7 UV–vis diffuse reflectance spectra (DRS) of undoped TNS and Ho-TNS



**Fig. 8** Fluorescence spectra of P25, undoped TNS, and Ho-TNS under excitation of 205 nm



**Fig. 9** Adsorption capacity of undoped TNS and Ho-TNS under 20 mg/L RhB in dark for 60 min

more electron–hole pairs than undoped TNS under the same irradiation.

Fluorescence spectra have been widely used to investigate the efficiency of charge carrier trapping, immigration, transferring, and the fate of electron–hole pairs in semiconductor particles [38, 39]. As FL emission mainly results from the recombination of excited electrons and holes, a lower FL intensity indicates a lower recombination rate of electron–hole and higher separation efficiency under the same test conditions [27]. Figure 8 shows the FL spectra of undoped TNS and Ho-TNS with different Ho/Ti ratios. These four FL signals are due to excitonic FL, which mainly result from surface oxygen vacancies and defects of the samples. The FL peaks at 451 and 468 nm are attributed to band edge free excitons, and other two peaks at 483 and 493 nm are attributed to bound excitons [40, 41]. The

suppression of FL intensity is obtained with the increasing Ho content. It demonstrates that Ho located on surface may act as electron-trapped agents and thus promote electron separation and transfer effects.

From the above results, we can draw a conclusion that with increasing Ho content, the specimens exhibit higher electron–hole separation efficiency, and their absorption edges shift to a longer wavelength. Meanwhile, the formation of TNS is delayed and the  $S_{\text{BET}}$  of specimens decrease. These results imply the existence of an optimal concentration of Ho to reach the best photoactivity.

#### Adsorption capacity and photocatalytic performance evaluations

The adsorption capacities of specimens under 20 mg/L RhB are shown in Fig. 9. The adsorption capacities drop rapidly after Ho doping. This phenomenon might be ascribed to the decrease of  $S_{\text{BET}}$ , which may reduce the opportunities for RhB molecules to contact with specimens. In addition, the formed Ho–O–Ti bonds located on the surface may change the surface charge distribution. Thanks to RhB molecules showing electropositivity in aqueous solution, the enhancement of absorption capacity of undoped TNS is accomplished via adsorbing opposite charged molecules. The formed Ho–O–Ti bonds weaken the electronegativity of specimens, which will lead to the reduction of adsorption capacities. Both reasons attribute to Ho doping, suggesting that Ho doping can reduce the adsorption capacities of specimens and alter the surface structure of specimens.

Photoactivities of specimens were estimated by measuring the degradation rate of RhB under UV–vis or visible light irradiation. Figure 10a shows that when the doping ratio is low (<1.0 %), the UV–vis photoactivity is positively related to doping ratio, and reaches the maximum with 1.0 % dosage. However, the photoactivity decreases rapidly when the doping ratio is more than 1.0 %. The photocatalytic degradation of RhB is a pseudo-first-order reaction, and its kinetics equation may be expressed by  $-\ln(C_t/C_0) = Kt$ , where  $K$  is reaction rate constant, and  $C_0$  and  $C_t$  are the concentration of RhB at the beginning of illumination and the reaction concentration at the time  $t$ , respectively.

The reaction rate constants ( $K$ ) have been calculated, and the results are shown in Fig. 10c. The  $K$  values indicate that the photocatalytic degradation rate of the 1.0 % Ho-doped TNS is 1.67 times of that of undoped TNS and 3.94 times of that of P25, respectively. Moreover, Fig. 10b and d shows the visible light photoactivity, which exhibits a very similar change trend with the increasing Ho ion content. The photocatalytic degradation rate of the 1.0 % Ho-TNS is 1.90 times of that of undoped TNS and 12.38 times of that of P25, respectively.



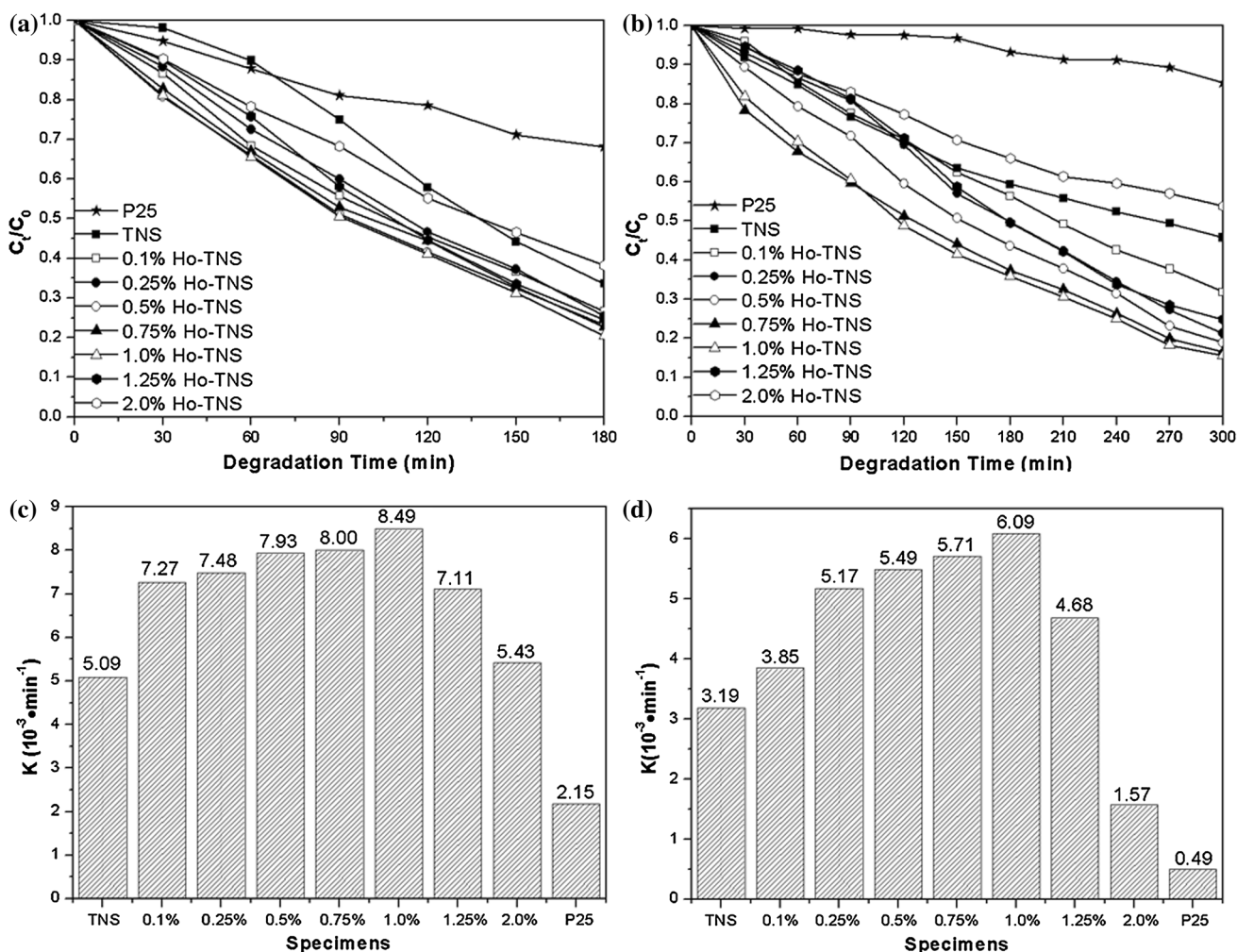


**Fig. 10** Photocatalytic degradation of RhB under UV-vis light (a) and visible light (b); the reaction rate constant ( $K$ ) values under UV-vis light (c) and visible light (d)

**Mechanism discussions**

The photoactivities of Ho-TNS may be affected by many variables, such as  $S_{BET}$  of specimens, the shift of adsorption edge, photogenerated electron-hole separation, and the change of adsorption capacity. Now we discuss how Ho have contributed to these variables and the possible mechanisms for the enhanced photoactivity of Ho-TNS. Under the hydrothermal conditions, Ho are mainly located on the surface of TNS and form Ho-O-Ti bonds. Then, Ho can impede the formation of nanosheets, which will lead to the reduction of their  $S_{BET}$ . The formed Ho-O-Ti bonds will change the charge distribution on the surface of specimens. Consequently, the adsorption capacities of specimens decrease rapidly. They would have negative effect on photoactivities of specimens. However, FL and DRS spectra indicate that Ho doping can promote electron separation effects and red-shift absorption edges. These

phenomena can be explained by electron transfer mechanisms. As self-sensitive dyes, after irradiation, the RhB\* molecules (excited RhB) chemisorbed on the surface of photocatalysts may inject electrons into the conduction band of  $TiO_2$ , which can lead to the visible photoactivity of undoped TNS, as illustrated in Fig. 11 (pathway I). The electron transfer mechanisms are different under visible light and UV light, for electrons cannot be excited from the valence bands of Ho-TNS into conduction bands directly merely under visible light irradiation. When visible irradiation is imposed, electrons can be excited by visible light from the valence bands into Ho 4f levels at first which is located just below Ti 3d levels. Then, they are excited into conduction bands of Ho-TNS (pathway II). This process can decrease the band-gap of specimens and lead to the red-shift of absorption edge, which are in accordance with the DRS data. In addition, Ho can be used as electron traps for the reason that the Ho contains incomplete 4f orbitals,

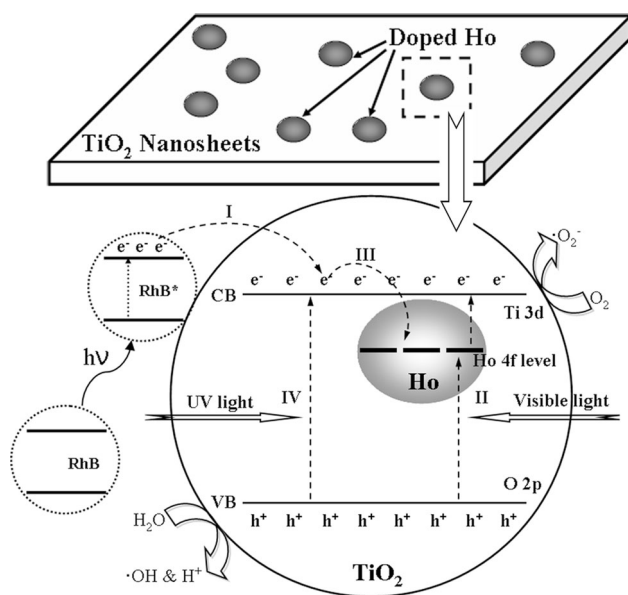


**Fig. 11** The possible electron transfer mechanisms of Ho-TNS

which can trap photogenerated electrons (pathway III). Because the capacity of Ho 4f level to capture electrons is relatively weak, the electron transfer between self-sensitive RhB\* and Ho 4f level would not take place, and the high doping amount (2.0 %) would not cause too much recombination centers for photogenerated electrons. This process indicates that Ho doping can promote electron separation and transfer effects, which are in agreement with FL spectra. When UV irradiation is imposed, apart from the existence of the three pathways discussed above, electrons can also be excited from the valence bands of Ho-TNS into conduction bands directly (pathway IV). In summary, the photoactivity of specimens may be affected by above mentioned variables. The effects of variables play different roles in photocatalytic process with different Ho doping ratios. When the doping ratio is low (<1.0 %), the enhanced electron–hole separation and the red-shift of adsorption edge play dominant roles, so the photoactivities of Ho-TNS increase. However, when the doping ratio is above 1.0 %, the effects of the decreased  $S_{\text{BET}}$  and adsorption capacities will reduce the photoactivities of specimens. Thus, the change trend of photoactivity can be observed in Ho-TNS under UV–vis light and visible light irradiation.

## Conclusions

In our study, Ho-TNS was prepared via a simple hydrothermal method using Degussa P25 and Ho nitrate. Ho doping was conducted in the formation process of TNS and formed Ho–O–Ti bonds on the surface. Ho doping can

affect the transformation from  $\text{TiO}_2$  to  $\text{H}_2\text{Ti}_3\text{O}_7$  and the formation of nanosheets. After Ho doping, the specimens have high electron–hole separation efficiency and their absorption edges shift to a longer wavelength, band-gap reduces from 3.18 to 3.07 eV; however, the  $S_{\text{BET}}$  and adsorption of RhB decrease. These phenomena are attributed to the electron transfer mechanisms and the inhibited transformation from  $\text{TiO}_2$  to  $\text{H}_2\text{Ti}_3\text{O}_7$ . The specimen with a doping ratio of 1.0 % (molar ratio) reaches the best photoactivity for degrading RhB, which is 1.67-fold and 3.94-fold higher compared with undoped TNS and P25 under UV–vis light, and 1.90-fold and 12.38-fold higher compared with undoped TNS and P25 under visible light, respectively. With this superiority, the photocatalyst may have a good application prospect in dealing with dye wastewater.

**Acknowledgements** This work was financially supported by the National Basic Research Program of China (973 Program, No. 2009CB939704 and No. 2009CB939705), the National Natural Science Foundation of China (No. J1210061), and the Large-scale Instrument and Equipment Sharing Foundation of Wuhan University (No. LF20120183).

## References

- Chen X, Mao SS (2007) Titanium dioxide nanomaterials: synthesis, properties, modifications, and applications. *Chem Rev* 107(7):2891–2959. doi:10.1021/cr0500535
- Fujishima A, Zhang XT, Tryk DA (2008)  $\text{TiO}_2$  photocatalysis and related surface phenomena. *Surf Sci Rep* 63(12):515–582. doi:10.1016/j.surfrep.2008.10.001
- Liu G, Wang LZ, Yang HG, Cheng HM, Lu GQ (2010) Titania-based photocatalysts-crystal growth, doping and heterostructuring. *J Mater Chem* 20(5):831–843. doi:10.1039/b909930a
- Lan Y, Gao XP, Zhu HY, Zheng ZF, Yan TY, Wu F, Ringer SP, Song DY (2005) Titanate nanotubes and nanorods prepared from rutile powder. *Adv Funct Mater* 15(8):1310–1318. doi:10.1002/adfm.200400353
- Cozzoli PD, Kornowski A, Weller H (2003) Low-temperature synthesis of soluble and processable organic-capped anatase  $\text{TiO}_2$  nanorods. *J Am Chem Soc* 125(47):14539–14548. doi:10.1021/ja036505h
- Zhou W, He Y (2012) Ho/ $\text{TiO}_2$  nanowires heterogeneous catalyst with enhanced photocatalytic properties by hydrothermal synthesis method. *Chem Eng J* 179:412–416. doi:10.1016/j.cej.2011.10.094
- Albu SP, Ghicov A, Macak JM, Hahn R, Schmuki P (2007) Self-organized, free-standing  $\text{TiO}_2$  nanotube membrane for flow-through photocatalytic applications. *Nano Lett* 7(5):1286–1289. doi:10.1021/nl070264k
- Nakahira A, Kubo T, Numako C (2010) Formation mechanism of  $\text{TiO}_2$ -derived titanate nanotubes prepared by the hydrothermal process. *Inorg Chem* 49(13):5845–5852. doi:10.1021/ic9025816
- Chen F, Liu Z, Liu Y, Fang P, Dai Y (2013) Enhanced adsorption and photocatalytic degradation of high-concentration methylene blue on  $\text{Ag}_2\text{O}$ -modified  $\text{TiO}_2$ -based nanosheet. *Chem Eng J* 221:283–291. doi:10.1016/j.cej.2013.02.019
- Chen F, Fang P, Gao Y, Liu Z, Liu Y, Dai Y (2012) Effective removal of high-chroma crystal violet over  $\text{TiO}_2$ -based nanosheet

- by adsorption–photocatalytic degradation. *Chem Eng J* 204–206:107–113. doi:10.1016/j.cej.2012.07.030
11. Li D, Yang F, Cheng H, Liu C, Sun M, Wu K, Ai M (2013) Protective effects of total flavonoids from *Flos Puerariae* on retinal neuronal damage in diabetic mice. *Mol Vis* 19:1999–2010
  12. Liu ZY, Sun DDL, Guo P, Leckie JO (2007) An efficient bicomponent TiO<sub>2</sub>/SnO<sub>2</sub> nanofiber photocatalyst fabricated by electrospinning with a side-by-side dual spinneret method. *Nano Lett* 7(4):1081–1085. doi:10.1021/nl061898e
  13. Yao BD, Chan YF, Zhang XY, Zhang WF, Yang ZY, Wang N (2003) Formation mechanism of TiO<sub>2</sub> nanotubes. *Appl Phys Lett* 82(2):281–283. doi:10.1063/1.1537518
  14. Matsumoto Y, Koinuma M, Iwanaga Y, Sato T, Ida S (2009) N doping of oxide nanosheets. *J Am Chem Soc* 131(19):6644–6645. doi:10.1021/ja807388t
  15. Cai SW, Hang WX, Xiong ZT, Ye FY, Ren C, Xu ZR, Liu C, Deng SQ, Zhao J (2013) Comparative study of root growth and sucrose-cleaving enzymes in metalliculous and non-metalliculous populations of *rumex dentatus* under copper stress. *Ecotox Env Safe* 98:95–102. doi:10.1016/j.ecoenv.2013.09.017
  16. Zhang Z, Long J, Xie X, Zhuang H, Zhou Y, Lin H, Yuan R, Dai W, Ding Z, Wang X, Fu X (2012) Controlling the synergistic effect of oxygen vacancies and N dopants to enhance photocatalytic activity of N-doped TiO<sub>2</sub> by H<sub>2</sub> reduction. *Appl Catal A* 425–426:117–124. doi:10.1016/j.apcata.2012.03.008
  17. Baker DR, Kamat PV (2009) Photosensitization of TiO<sub>2</sub> nanostructures with CdS quantum dots: particulate versus tubular support architectures. *Adv Funct Mater* 19(5):805–811. doi:10.1002/adfm.200801173
  18. Primo A, Corma A, Garcia H (2011) Titania supported gold nanoparticles as photocatalyst. *Phys Chem Chem Phys* 13(3):886–910. doi:10.1039/c0cp00917b
  19. Liang CH, Li FB, Liu CS, Lu HL, Wang XG (2008) The enhancement of adsorption and photocatalytic activity of rare earth ions doped TiO<sub>2</sub> for the degradation of orange I. *Dyes Pigments* 76(2):477–484. doi:10.1016/j.dyepig.2006.10.006
  20. Kim S, Hwang SJ, Choi WY (2005) Visible light active platinumion-doped TiO<sub>2</sub> photocatalyst. *J Phys Chem B* 109(51):24260–24267. doi:10.1021/jp055278y
  21. Klosek S, Raftery D (2001) Visible light driven V-doped TiO<sub>2</sub> photocatalyst and its photooxidation of ethanol. *J Phys Chem B* 105(14):2815–2819. doi:10.1021/jp004295e
  22. Bingham S, Daoud WA (2011) Recent advances in making nano-sized TiO<sub>2</sub> visible-light active through rare-earth metal doping. *J Mater Chem* 21(7):2041–2050. doi:10.1039/c0jm02271c
  23. Parida KM, Sahu N (2008) Visible light induced photocatalytic activity of rare earth titania nanocomposites. *J Mol Catal* 287(1–2):151–158. doi:10.1016/j.molcata.2008.02.028
  24. El-Bahy ZM, Ismail AA, Mohamed RM (2009) Enhancement of titania by doping rare earth for photodegradation of organic dye (direct blue). *J Hazard Mater* 166(1):138–143. doi:10.1016/j.jhazmat.2008.11.022
  25. Shi Z, Xiang Y, Zhang X, Yao S (2011) Photocatalytic activity of Ho-doped anatase titanium dioxide coated magnetite. *Photochem Photobiol* 87(3):626–631. doi:10.1111/j.1751-1097.2011.00893.x
  26. Liu Y, Fang P, Cheng Y, Gao Y, Chen F, Liu Z, Dai Y (2013) Study on enhanced photocatalytic performance of cerium doped TiO<sub>2</sub>-based nanosheets. *Chem Eng J* 219:478–485. doi:10.1016/j.cej.2012.12.098
  27. Cai H, Liu G, Lü W, Li X, Yu L, Li D (2008) Effect of Ho-doping on photocatalytic activity of nanosized TiO<sub>2</sub> catalyst. *J Rare Earth* 26(1):71–75. doi:10.1016/s1002-0721(08)60040-x
  28. Chen Q, Zhou W, Du G, Peng L (2002) Trititanate nanotubes made via a single alkali treatment. *Adv Mater* 14:1208–1211
  29. Alvarez-Ramirez F, Ruiz-Morales Y (2007) Ab initio molecular dynamics calculations of the phase transformation mechanism for the formation of TiO<sub>2</sub> titanate-type nanosheets from anatase. *Chem Mater* 19(12):2947–2959. doi:10.1021/Cm062162l
  30. Ohsaka T, Izumi F, Fujiki Y (1978) Raman spectrum of anatase TiO<sub>2</sub>. *J Raman Spectrosc* 7:321–324
  31. Yoshida K, Miao L, Tanaka N, Tanemura S (2009) Direct observation of TiO<sub>6</sub> octahedron forming titanate nanotube by advanced transmission electron microscopy. *Nanotechnology* 20(40):405709. doi:10.1088/0957-4484/20/40/405709
  32. Gao T, Fjellvag H, Norby P (2008) Raman scattering properties of a protonic titanate H<sub>x</sub>Ti<sub>2-x/4</sub> square O-x/4(4)center dot H<sub>2</sub>O (square, vacancy; x = 0.7) with lepidocrocite-type layered structure. *J Phys Chem B* 112(31):9400–9405. doi:10.1021/jp801639a
  33. Liu FM, Wang TM (2002) Surface and optical properties of films grown by radio frequency nanocrystalline anatase titania reactive magnetron sputtering. *Appl Surf Sci* 195(1–4):284–290. doi:10.1016/s0169-4332(02)00569-x
  34. Schroeder T, Lupina G, Dabrowski J, Mane A, Wenger C, Lippert G, Mussig HJ (2005) Titanium-added praseodymium silicate high-k layers on Si(001). *Appl Phys Lett* 87(2):022902. doi:10.1063/1.1978978
  35. Pan T, Yen L, Hu C, Chao T (2010) Structural and electrical properties of high-k HoTiO<sub>3</sub> gate dielectrics. In: Gusev EP, Kwong DL, Roozeboom F et al (eds) *Advanced gate stack, source/drain, and channel engineering for Si-based Cmos 6: new materials, processes, and equipment*, vol 28. ECS transactions, vol 1. Electrochemical Soc Inc, Pennington, pp 241–245. doi:10.1149/1.3375607
  36. Shi J, Zheng J, Hu Y, Zhao Y (2011) Photocatalytic degradation of organic compounds in aqueous systems by Fe and Ho codoped TiO<sub>2</sub>. *Kinet Catal* 49(2):279–284. doi:10.1134/s002315840802016x
  37. Zhao W, Ma WH, Chen CC, Zhao JC, Shuai ZG (2004) Efficient degradation of toxic organic pollutants with Ni<sub>2</sub>O<sub>3</sub>/TiO<sub>2</sub>-xBx under visible irradiation. *J Am Chem Soc* 126(15):4782–4783. doi:10.1021/ja0396753
  38. Ren C, Yang B, Wu M, Xu J, Fu Z, lv Y, Guo T, Zhao Y, Zhu C (2010) Synthesis of Ag/ZnO nanorods array with enhanced photocatalytic performance. *J Hazard Mater* 182(1–3):123–129. doi:10.1016/j.jhazmat.2010.05.141
  39. Zhou W, Liu H, Wang J, Liu D, Du G, Cui J (2010) Ag<sub>2</sub>O/TiO<sub>2</sub> Nanobelts heterostructure with enhanced ultraviolet and visible photocatalytic activity. *ACS Appl Mater Inter* 2(8):2385–2392. doi:10.1021/am100394x
  40. Zhang W, Zhang M, Yin Z, Chen Q (2000) Photoluminescence in anatase titaniumdioxide nanocrystals. *Appl Phys B* 70:261–265. doi:10.1007/s003409900161
  41. Yu J, Yu J, Ho W, Jiang Z, Zhang L (2002) Effects of F-doping on the photocatalytic activity and microstructures of nanocrystalline TiO<sub>2</sub> powders. *Chem Mater* 14:3808–3816